JOURNAL OF MATERIALS SCIENCE 22 (1987) 947–961

Microstructural details and the effect of testing conditions on the fracture toughness of injection-moulded poly(phenylene-sulphide) composites

J. KARGER-KOCSIS*, K. FRIEDRICH
Polymer and Composites Group, Technical University Hamburg-Harburg, 2100 Hamburg 90, FRG

This paper deals with the microstructure–property relationships of particle toughened poly(phenylene-sulphide) (PPS) and of two short glass and carbon fibre reinforced PPS versions. The microstructural characterization of injection-moulded plaques was performed by the use of differential scanning calorimetry and scanning electron microscopy. Studies of the materials' fracture toughness using compact tension specimens, revealed a clear influence of the type of fibre reinforcement and of the external testing conditions, i.e. temperature, T, and loading rate, v. Failure mechanisms of the composite materials were analysed by fractographic studies in the SEM. The final presentation of the results was performed in terms of failure maps and fracture toughness–elastic modulus maps. The latter can be used by engineers or designers for a systematic material evaluation with respect to a certain property profile at defined external service conditions of T and v.

1. Introduction

Poly (p-phenylene sulphide) (PPS) is a versatile temperature and chemical resistant, inherently flame retardant semicrystalline engineering thermoplastic material. In spite of the fact that the first reports on the synthesis of PPS date back to the end of the last century [1, 2], which means PPS can be considered to be one of the oldest thermoplastic polymers, its commercialization by Phillips Petroleum Co. began rather late, i.e. in 1973 [3, 4]. For upgrading the moderate mechanical and, especially, the impact performance of the low molecular-weight PPS, curing was recommended. The curing is, in reality, a thermal process performed either in the solid (175 to 280° C) or the melt phase (315 to 425° C) and mostly in an air environment, the effect of which is an increase in molecular weight (melt viscosity) and a change in crystallinity. During the curing treatment rather complex chemical reactions occur simultaneously, such as chain extension, oxidative and thermal cross-linking, oxygen uptake, as demonstrated on PPS and its model compounds [5–8]. Recently, a new curing method in inert atmosphere by sulphur was reported to increase effectively the otherwise moderate impact resistance of PPS [9]. Upgrading of the mechanical properties is mostly studied as a function of the curing time and temperature [9, 10]. PPS is very sensitive to the processing parameters changing its thermal and, especially, crystallization behaviour [3, 4, 11], and several fundamental works on the crystallization kinetics of PPS have been published [12, 13].

The recent interest for PPS may be explained mostly by two reasons:

1. PPS is considered to be a proper candidate for replacing the conventional thermosetting resin matrices in composites, because one expects from its use easier processing methods of parts with more complicated shapes and a recyclability of lightweight advanced composities;

2. the electrical and thermal properties of PPS are very attractive for use in the electronic (wire coating) and micro-electronic industry (chip panel, encapsulation, integrated circuits etc.)

It is surprising, however, that on the first topic only a few works were published, some of them treating the structure–property relationships of short fibre reinforced PPS composites. These works yield information about the microstructure–fracture toughness relationships [14], lifetime measurements in corrosive media based on the fracture mechanics concept [15, 16] (stress corrosion crack propagation test), and morphological changes during curing [17]. To date no information is available on the change of the fracture toughness as a function of temperature, strain rate and solid-phase curing causing morphological alterations. These functions are, on the other hand, of basic importance since PPS, being a temperature-resistant thermoplastic, is often used at high service temperatures, at which solid phase curing, thermal ageing or annealing may alter the microstructure of the composite. A study on the strain rate effects as a function of temperature would yield valuable

*Alexander von Humboldt fellow; on leave from Taurus Hungarian Rubber Works, Budapest, Hungary.

0022–2461/87 $03.00 + .12

information about the impact characteristics of the composite.

The aim of the present paper is to contribute to the fracture mechanical characterization of PPS and its short glass (GF) and carbon fibre (CF) reinforced composites by investigating temperature, strain rate and annealing (curing) effects.

2. Experimental details

2.1. Materials

The materials investigated are based on Ryton PPS of Phillips Petroleum Co. Bartlesville, Oklahoma, USA. It was a first-generation low molecular weight grade since its composition was analysed as follows: C 66%, H 4.4%, S 27.2% and Cl 0.9%. Supposing that the chlorine was present only as endgroups, a chain of 70 to 100 units would give a reasonable agreement with the above results. The so-calculated M_n = (0.8 to 1) $\times$ 10^4 g, is lower than the generally supposed ones (1.5×10^4 g [13], 1.7×10^4 g [3]). The PPS was compounded and injection-moulded to rectangular plaques of about 6 mm thickness by LNP Engineering Plastics Inc., Malvern, Pennsylvania, USA. In addition to the neat polymer matrix material, two short fibre reinforced versions (30 wt % glass fibres GF; 30 wt % carbon fibres CF) were tested.

2.2. Microstructural characterization

The layer structure of the neat matrix and that of the matrices in the composites were characterized by means of differential scanning calorimetric (DSC) investigations. The DSC traces in various sections across the plaque thickness were recorded by a Heraeus DTA 500 modul connected to a TA 500S device with a heating range of 20° C min^{-1}. Heat effects were calibrated by the heat of fusion of ultrapure lead and tin.

The microstructure of the injection-moulded composite plaques was described in terms of a natural laminate, consisting of two skin (S) and one core (C) layers of different thickness, and by the average fibre orientation factor, f_p, in these regions (f_{ps} and f_{pc}, respectively). Fibre orientation was visualized on metallographically polished samples by high contrast imaging in the scanning electron microscope (SEM). Prior to SEM, the polished samples were gold sputtered in order to avoid electrical charging.

The average fibre orientation factor (f_p) was calculated using Equations 1a and b

$$f_p = 2\langle\cos^2\varphi\rangle - 1 \tag{1a}$$

$$\langle\cos^2\varphi\rangle = \frac{\sum_i N(\varphi_i)\cos^2(\varphi_i)}{\sum_i N(\varphi_i)} \tag{1b}$$

where φ_i is the angle between the individual fibres and the mould flow direction (MFD) and $N(\varphi_i)$ is the number of fibres under a certain angle φ_i. Additionally, the fibre length distribution was determined by means of light microscopy (LM), after burning off the matrix at about 700° C.

Values of the specimen density, obtained by weighting the samples hydrostatically, were used to calculate the reinforcing fibre volume fraction (V_F), according to Equation 2

$$V_F = \frac{\varrho_c - \varrho_M}{\varrho_F - \varrho_M} \tag{2}$$

where ϱ_c, ϱ_M and ϱ_F are the densities of the composite, matrix and fibre, respectively.

2.3. Thermal treatments

Annealing (solid-phase curing) of some specimens was performed at 230° C for 8 h in a circulating air thermostatic chamber. The annealing effects were followed by differential scanning calorimetry (DSC), infrared spectroscopy and a thermomechanical analyser (TMA). The infrared spectra were registered by a Perkin–Elmer device with the KBr technique using a fine scrap of the matrix and its composites. Thermomechanical curves were taken using a Heraeus TMA500 apparatus.

2.4. Fracture toughness measurements

CT specimens cut from the plaques were notched perpendicular to the MFD (T-notch, see Fig. 1). The initial notch was sharpened with a razor blade prior to the static loading experiments, which were performed on a Zwick 1445 type testing machine. Testing was carried out at different crosshead speeds (v) (10^0, 10^1, 10^2 and 10^3 mm min^{-1}). The test temperature (T) varied in a broad range (from -60 up to $+180$° C), and was set by the use of a thermostatic chamber. The calculation of the fracture toughness (K_c) was performed according to Equation 3

$$K_c = \frac{F_c}{BW} a_i^{1/2} f(a_i/W) \tag{3}$$

where F_c is the maximum load or the intercept of the 95% slope with the load–displacement curve, according to the ASTM E 399 standard, the latter evaluation was used only for specimens fractured at 180° C; B is specimen thickness ($\sim$6.4 mm); W is the specimen width (29 mm); a_i the actual crack length; $f(a_i/W)$ is the shape factor, as calculated from

$$f(a_i/W) = 29.6 - 185.5\left(\frac{a_i}{W}\right) + 655.7\left(\frac{a_i}{W}\right)^2 - 1017\left(\frac{a_i}{W}\right)^3 + 638.9\left(\frac{a_i}{W}\right)^4 \tag{4}$$

2.5. Fractography

The crack propagation path was visualized on microphotographs taken either at direct illumination by a Polyvar light microscope, or on scanning electron micrographs (Leitz SEM 1600T). The failure mode of the broken CT specimens was also studied by SEM. Prior to these SEM observations, the surfaces were coated with a thin gold layer, using a Leitz Sputtering Chamber, type 166.

3. Results and discussion

3.1. Microstructural details of the materials investigated

3.1.1. Morphology of the PPS matrices

Evidence of the layered structure of the matrix in the composites was obtained from DSC traces taken from

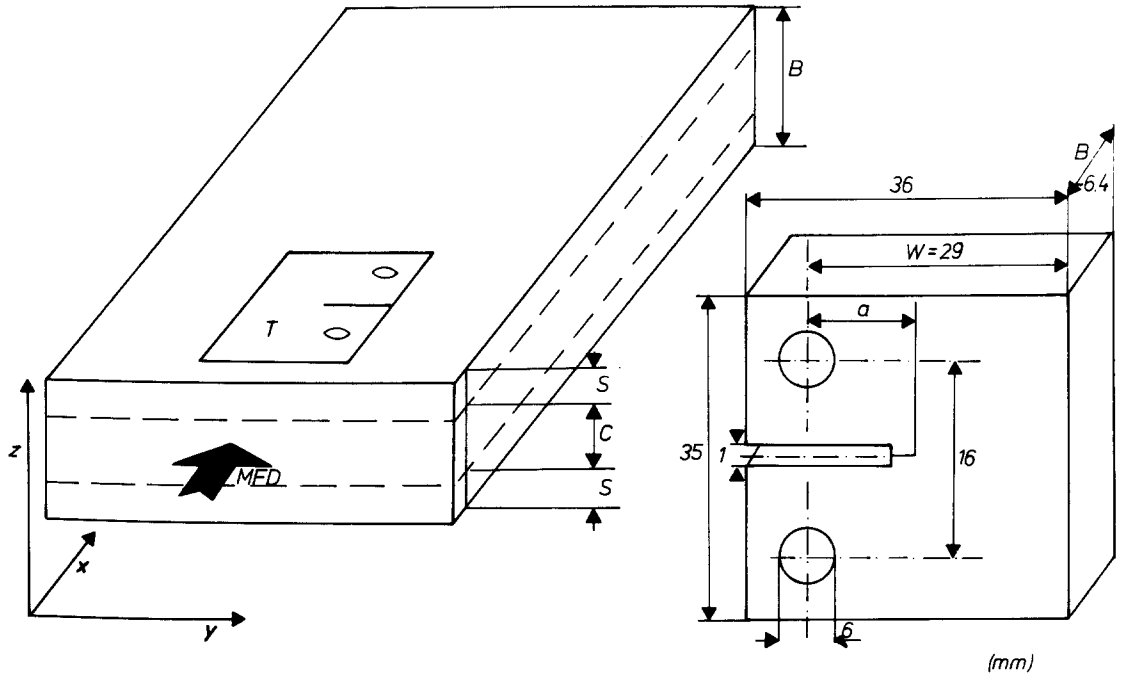

Figure 1 Specimen machining and geometry of the CT-specimen used.

various depths across the thickness of the injection moulded plaque. The as-moulded GF-PPS sample shows a three-layered matrix structure while that of the CF-reinforced composite shows a two-layer matrix structure (cf. curves 1a, 1b, and 1c in Figs 2 and 3). After annealing, the matrix in both systems exhibits a two-layer structure (cf. curves 2a and 2c in Figs 2 and 3).

In both composites the DSC traces of the surface layers (1a) indicate a fully amorphous region, since the glass transition (T_g) at $T = \sim 90°$ C and the recrystallization exotherm at $T = \sim 120°$ C are clearly perceptible. This means, that for the injection-moulding of the samples, the cold-mould process was used by the processor [4]. The T_g in these curves shows a characteristic enthalpy relaxation lacking in the inner regions (1b, 1c) which is linked to the free volume changes. The GF-reinforced composite shows two other peculiarities compared to the CF-PPS system. One is a small endothermic peak or a shoulder at $T = \sim 160°$ C, while the other is a new recrystallization exotherm at $T = \sim 245°$ C. Both can be attributed to the fact that the GF-PPS proved to be an impact-modified grade, based on scanning electron micrographs taken from the fracture surface (Fig. 4).

From the peak at $T = 160°$ C it can be assumed that the impact modifier used is probably a modified polypropylene. The recrystallization exotherm at $T = \sim 245°$ C, being present in both the shear (b) and core (c) region of the matrix may be explained by the variation in elasticity of the PPS melt caused by the impact modifier and its good adhesion to the PPS matrix. It is rather accepted that in change elasticity of the melt due to the presence of toughening particles less stiff than the polymer matrix may cause a big change in the layered structure of the blend [18, 19]. In our case this effect should be highly pronounced since the matrix is a very low molecular weight (M_n) polymer.

The micrographs in Fig. 4 also indicate a good adhesion between the modifier particles and the matrix. This is generally achieved by a grafted modifier, the grafted segments of which can penetrate into the surrounding polymer matrix thus yielding a locally "stretched" state of the matrix around the particles. Supposing such an effect exists, a reasonable explanation is given as to why the matrix is found in a frozen stress state hindering the crystallization up to a temperature range close to the melt temperature of the PPS-matrix ($T_m = 270°$ C).

The differences between GF-PPS and CF-PPS almost disappear after annealing the samples at 230° C for 8 h. Instead, both materials exhibit a double melting characteristic (Figs 2 and 3). The first premelting peak at $T = \sim 245°$ C, i.e. near to the annealing temperature, is followed by the main melting at $T = \sim 270°$ C. The premelting is more characteristic for the skin and shear layer than for the core (cf. Table I). Double melting for PPS was first reported based on DTA results [7] probably caused by the thermal process during preparation. The melting peak at $T = \sim 270°$ C for both the as-moulded and annealed samples is smaller than the reported one ($T_m = 285°$ C [3, 20], $T_m = 295°$ C [21]) which may be explained here by the presence of smaller PPS crystallites, due to the nucleating effect of the reinforcing fibres [17].

The increased density of the PPS matrix in the neat and reinforced samples, as well as the increase of the heat of fusion (cf. Table I), can be attributed to the perfection of the crystallites during annealing [22, 23]. This is contrary to the finding of Brady [4] who emphasized that annealing conducted below T_m has no or little effect on the crystallinity of PPS. Our results are also in contradiction with the conclusion of Zeng and Ho [17] who claimed that a solid-state annealing yields a lower degree of crystallinity. Accepting 80 J g^{-1} for the melt enthalpy of the 100% crystalline PPS (recently proposed by Lovinger *et al.* [13]), a relative increase in crystallinity of 45 to 87% could be

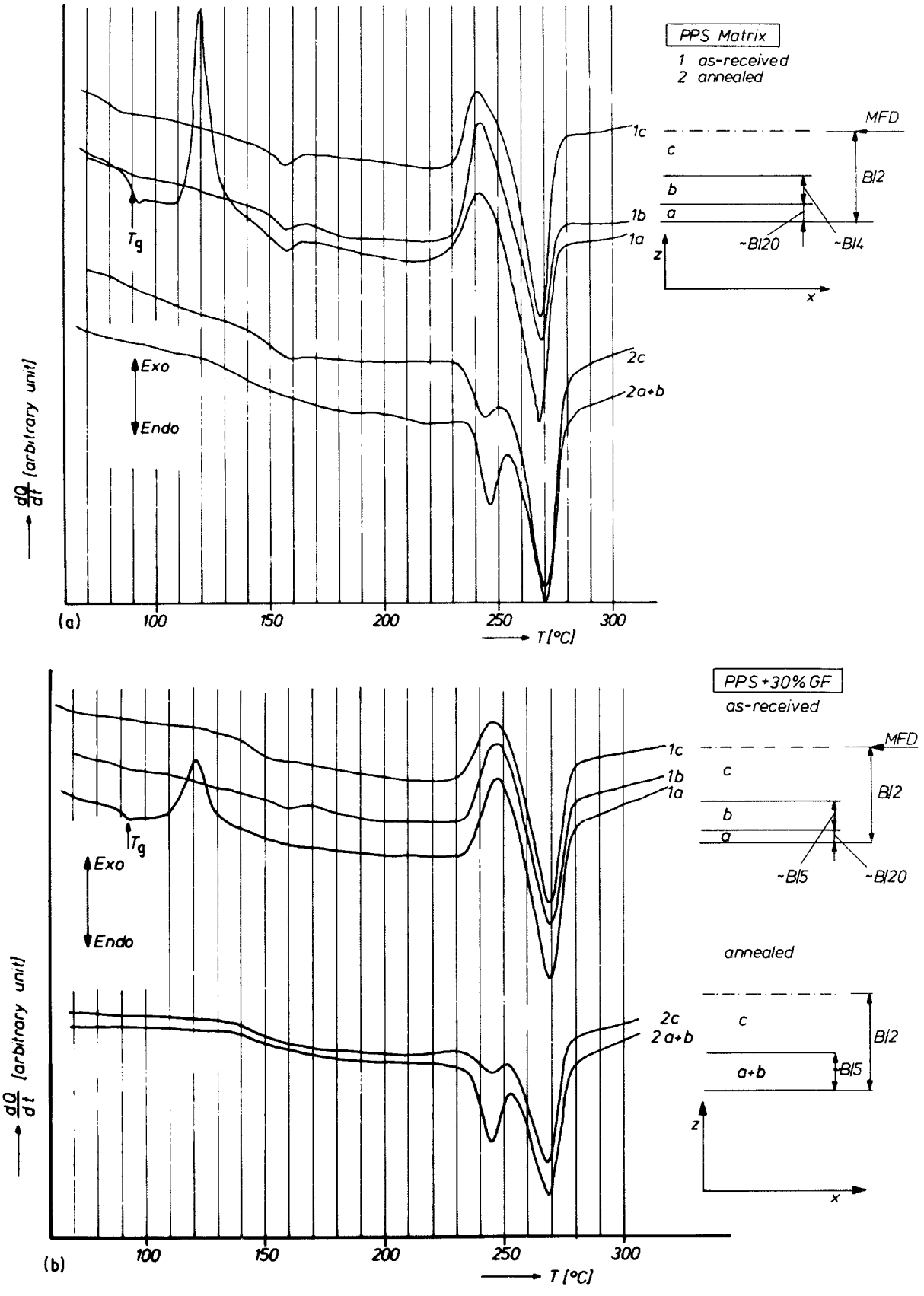

Figure 2 (a) DSC traces from various depth of the thickness (B) of the as-moulded (1) and annealed (2) PPS matrix. (b) DSC traces from various depth of the thickness (B) of the as-moulded (1) and annealed (2) GF-reinforced PPS illustrating the matrix layer structure.

detected from the DSC thermograms of the neat and reinforced PPS samples, when comparing the as-moulded and annealed conditions. Since the recrystallization exotherm at $T = \sim 245°\,C$ overlapped that of the melting endotherm at $T = \sim 270°\,C$, the crystalline proportion was calculated from the crystallization exotherm, registered in the cooling regime of the previously melted samples. The overlapping DSC peaks were resolved by a trial and error curve fitting method for quantifying the heat effects. It should be noted here that the crystallinity values calculated from density measurements using 1.43 and 1.32 $g\,cm^{-3}$ crystallographic densities for the fully crystalline and amorphous PPS, respectively [21], are much lower

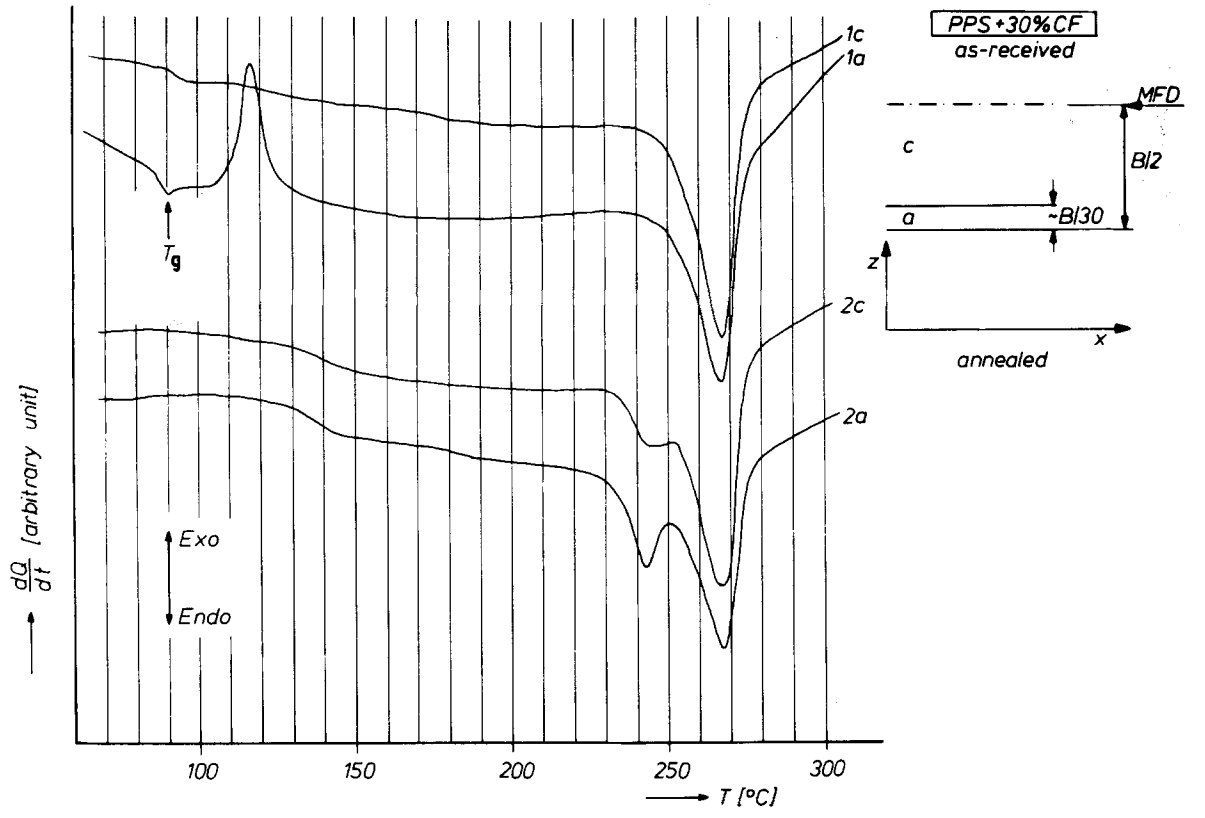

Figure 3 DSC traces from various depth of the thickness (B) of the as-moulded (1) and annealed (2) CF-reinforced PPS illustrating the matrix layer structure.

TABLE I Microstructural characterization of the matrix in the neat and reinforced injection-moulded PPS samples (all enthalpy values are related to the neat matrix)

Morphology, thermal property	Neat PPS*		Reinforced PPS			
	As-moulded	Annealed	30% GF*		30% CF	
			As-moulded	Annealed	As-moulded	Annealed
skin, a (mm)	$\sim B/20$	$\sim B/4$	$\sim B/20$	$\sim B/5$	$\sim B/30$	$\sim B/30$
shear zone, b (mm)	$\sim B/4$		$\sim B/5$			
Recrystallization enthalpy, ΔH_{rc} ($J\,g^{-1}$)						
at $T = 120°C$ in the a zone	16	–	11	–	13	–
at $T = 245°C$ in the a zone	9	–	10	–	–	
Melt enthalpy, ΔH_m ($J\,g^{-1}$):						
at $T = 275°C$ in the a zone	21	–	21	–	30	–
Ratio of ΔH_{rc} at $T = 245°C$ to ΔH_m at $T = 275°C$ (%)						
in the b region	40–50	–	55–60	–	–	–
in the c region	40–45	–	45–50	–	–	–
Overall melt enthalpy, ΔH_{mT} ($J\,g^{-1}$) of the annealed samples	–	41	–	46	–	51
Part of the premelting at $T = \sim 245°C$ to that of ΔH_{mT} (%)						
in the $a(+b)$ region	–	20–22	–	20–25	–	20–25
in the c region	–	12–15	–	10–13	–	13–16
Average crystallization enthalpy (ΔH_c) during cooling ($J\,g^{-1}$)	28		25		29	
DSC crystallinity from the ΔH_c and ΔH_{mT} values, respectively (%)	35	51	31	58	36	64
Measured density ($g\,cm^{-3}$)	1.32	1.36	1.54	1.57	1.43	1.45

*Impact modified matrix.

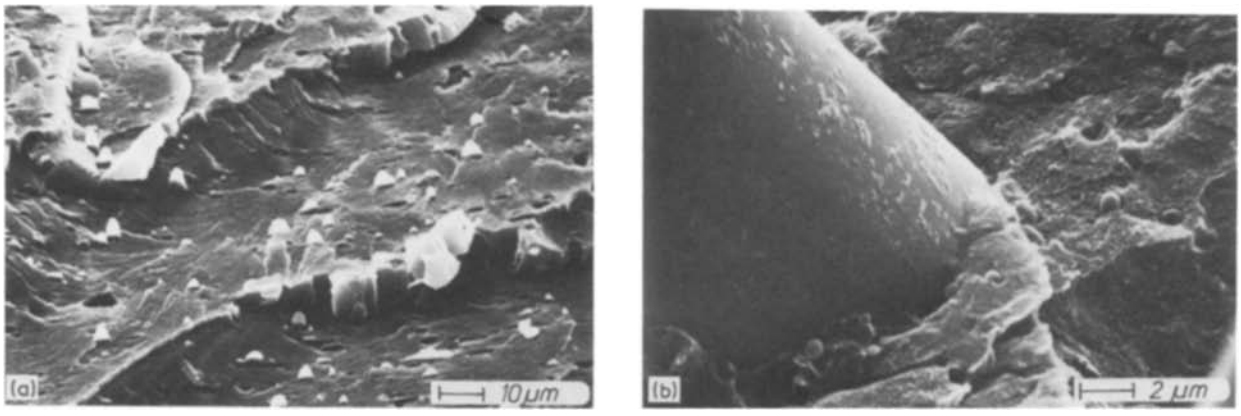

Figure 4 SEM micrographs on the fracture surface of the impact modified PPS matrix (a) and GF-reinforced PPS composite (b).

than the DSC crystallinities. But this is due to the fact that the materials contained various internal voids (which are seen in the micrograph of Fig. 5).

The question, whether the matrix became crosslinked or not during heat treatment could be answered by the use of a TMA device. The TMA spectra, which are sensitive to the molecular weight alteration [10, 24], indicated no change in the melt viscosity because the slope of the curves in the melt range was the same before and after annealing. The main argument, however, that no crosslinking occurred originated from the infrared spectra. These did not show any increases in the characteristic vibration for the trisubstituted (860 cm^{-1}) benzene rings. Also, no changes in intensity or shifts in the umbrella vibration of the p-disubstituted benzene ring (810 cm^{-1}) were observed.

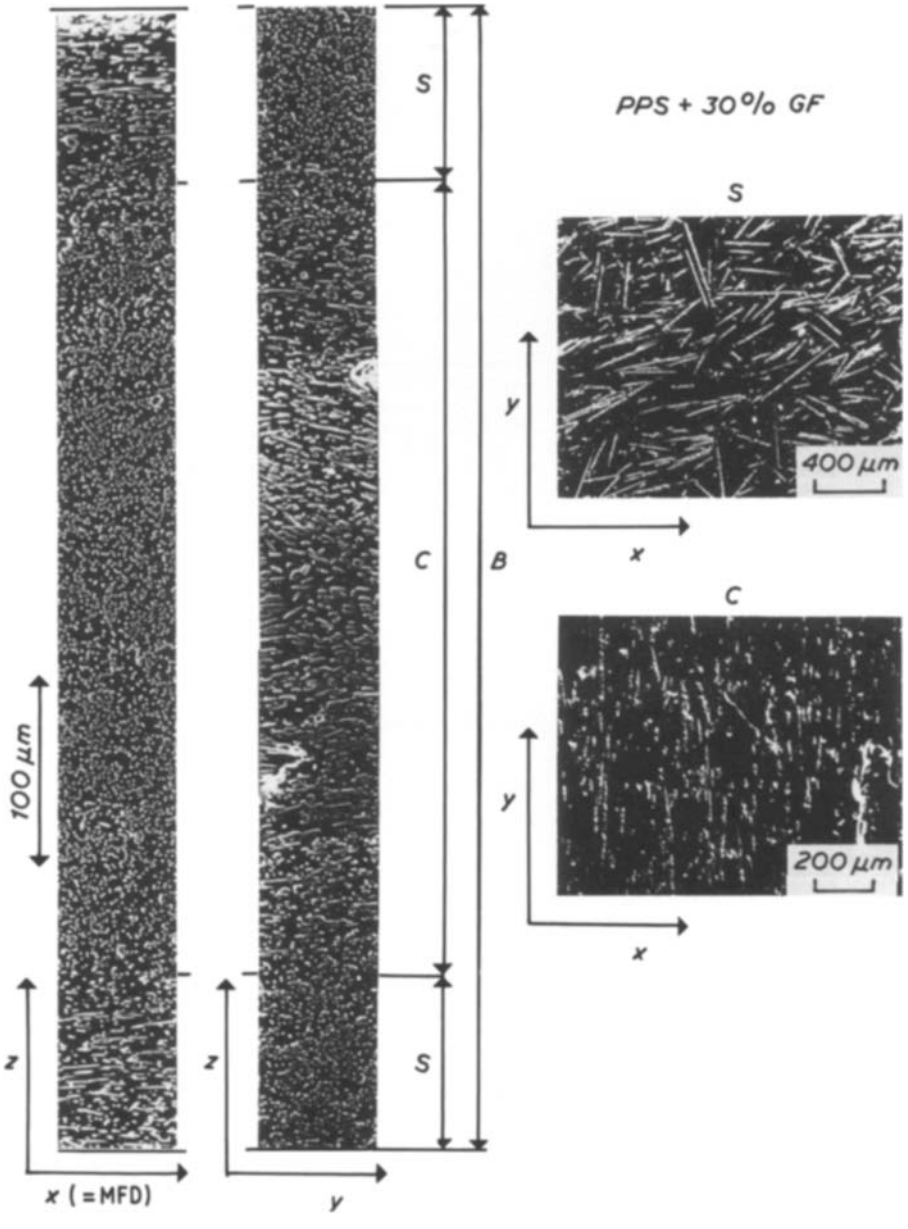

Figure 5 Composed SEM micrograph of the reinforcement layer structure of the GF-PPS composite in the z-(x, y) and y-x planes in the skin (S) and core (C) regions, respectively.

TABLE II Microstructure of the PPS composites (thickness $B = \sim 6.4$ mm)

Parameter, property	PPS + 30% GF	PPS + 30% CF
Layer structure:		
$2S/B$	0.31	0.35
C/B	0.69	0.65
Fibre orientation:		
$f_{P,S}$	0.52	0.66
$f_{P,C}$	−0.92	−0.94
Fibre characteristics:		
Average fibre length (μm)	180	100
Aspect ratio	18–20	10–13
Fibre volume fraction* (vol %)	18.5	22.8

*Supposing an average density of 1.35 g cm^{-3}, found for semicrystalline PPS and 2.55 and 1.96 g cm^{-3} for the GF and CF, respectively.

3.1.2. Arrangement of fibres in the composites

An example of the fibre orientation distribution across the plaque thickness of GF-PPS is represented in Fig. 5. Roughly, a natural laminate consisting of three major layers of different fibre orientation can be identified. In the two surface layers (S) fibres are oriented preferrably parallel to the mould fill direction (MFD) whereas the opposite is observed for the core layer (C). The absolute value of the average fibre orientation factor in the core ($f_{p,c}$) was much higher than that of the skin ($f_{p,s}$) (Table II). This is different from the trend often observed for injection-moulded plaques of about 3 mm thickness, in which the absolute f_p values are almost the same, but with an opposite sign for the S and C regions, respectively [14]. In the present case, the plaque thickness of $B = \sim 6$ mm results in ratios of C/B greater than $2S/B$, which probably allows a stronger elongational flow, resulting in a high fibre orientation perpendicular to the MFD in the mid region [25]. The more parallel alignment of the carbon compared to the glass fibres in the S-zone, may probably be attributed to both the more viscous nature of the unmodified PPS melt and the fact that the lighter carbon fibres are tilted more easily to the MFD by the shear field in the skin region. An additional effect might arise from the narrower fibre length distribution in the CF-PPS material, in which at the same time, the average fibre length is somewhat smaller than in case of the GF reinforcement (Fig. 6).

The fibre volume fraction (V_F) calculated from the measured densities (Table I) by Equation 2 is also smaller than that reported in Table II because of the internal voids of the matrix.

3.2. Stiffness and fracture toughness as a function of external testing conditions

From the load-displacement curves registered during loading of the CT-specimens, the initial slope (E_{in}, N m^{-1}), and the area under the curve up to F_c(A_c, N m) were read and calculated. E_{in} is an indirect measure for the "elastic modulus" of the material (E), F_c correlates with the material's "fracture toughness" (K_c), and A_c can be treated as the "work of failure initiation" (W), as long as both the CT-specimen geometry and the razor notch extension remain constant [26].

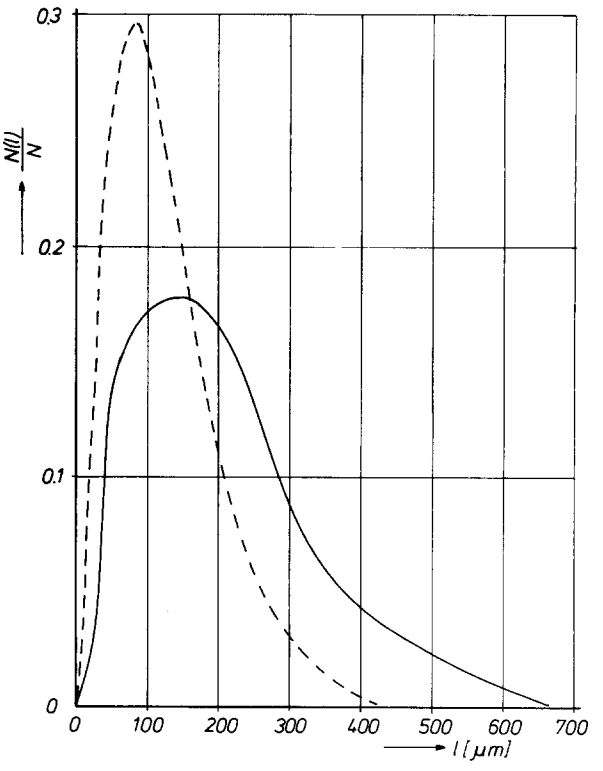

Figure 6 Fibre length distribution in the as-moulded PPS composites. (——) 30% GF-PPS, (– – –) 30% CF-PPS.

For the neat PPS-matrix material, E_{in} and K_c have been measured over a wide range of temperatures at a crosshead speed of $v = 10^0$ mm min^{-1}. The results are illustrated in Fig. 7. While the "modulus" E_{in} showed a clear drop when exceeding the glass transition temperature at around 90° C, this effect was not measurable for the fracture toughness K_c. Its values increased in a nearly linear manner from 0.65 MPa m$^{1/2}$ at $T = -60°$ C up to about 1.05 MPa m$^{1/2}$ at $T = 180°$ C.

The trend of E_{in} with T, shown for the PPS-matrix in Fig. 7, is also reflected in case of the two short fibre reinforced PPS versions (Figs 8a and b). Of course, the absolute values of E_{in} are higher for the composites relative to those of the unreinforced PPS-material. A carbon fibre was a little superior to a glass fibre reinforcement in this respect. For both material groups and at each temperature level, the values of E_{in} increase only slightly with the testing velocity applied (at least in the range between 10° to 10^3 mm min^{-1}).

This fact is, however, not true for the measured fracture toughness data of the composites (Figs 9a and b). At higher testing velocities, in particular, a clear reduction in K_c is detected. As an example, this is shown in the form of a K_c against log v diagram for the room-temperature testing conditions in Fig. 9c. The other differences found in Figs 9a and b relative to the K_c–T curve of the unreinforced PPS-matrix (Fig. 7) are more irregularly shaped curves with a preferred tendency towards decreasing K_c with increasing T. Both observations can be attributed to the fact that the fracture toughness of the fibre reinforced polymers is not only determined by the failure behaviour of the polymer matrix but also, more or less, by

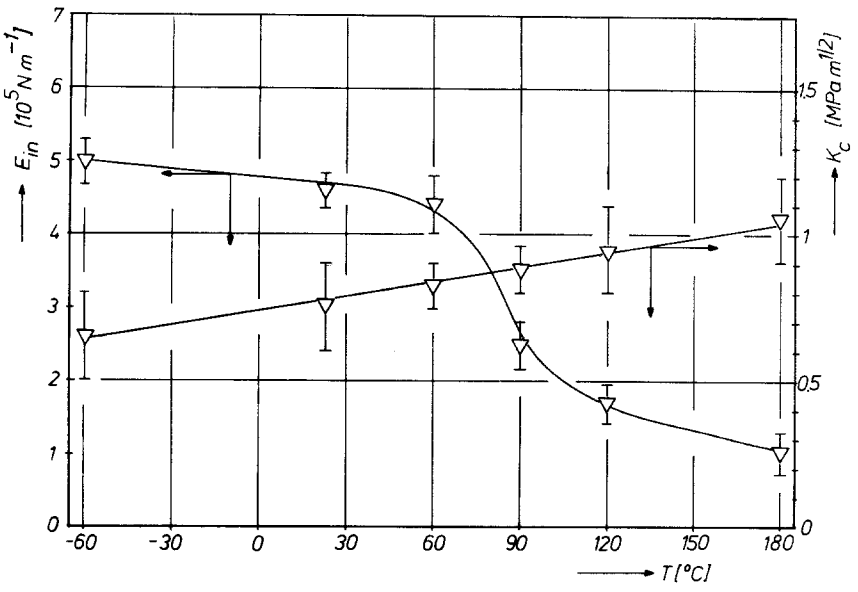

Figure 7 E_{in} against T and K_c against T curves for (▽) the PPS matrix at $v = 10^0$ mm min^{-1}, and the T-crack.

those mechanisms of energy absorption introduced by the different types of fibres.

Strictly speaking, a direct comparison between the unreinforced and reinforced versions may be performed only for the glass reinforced PPS, because in this case the matrix is of the same, impact-modified type as the unreinforced material itself (not valid for the CF-PPS composite). In normalized form, this is demonstrated in Figs 10a and b for the elastic modulus (E^*) and the fracture toughness (K_c^*), respectively. While the modulus of the composite at each temperature level is always higher by a factor of about 2 than that of the matrix polymer (Fig. 10a), this constant difference factor is not observed for the fracture toughnesses.

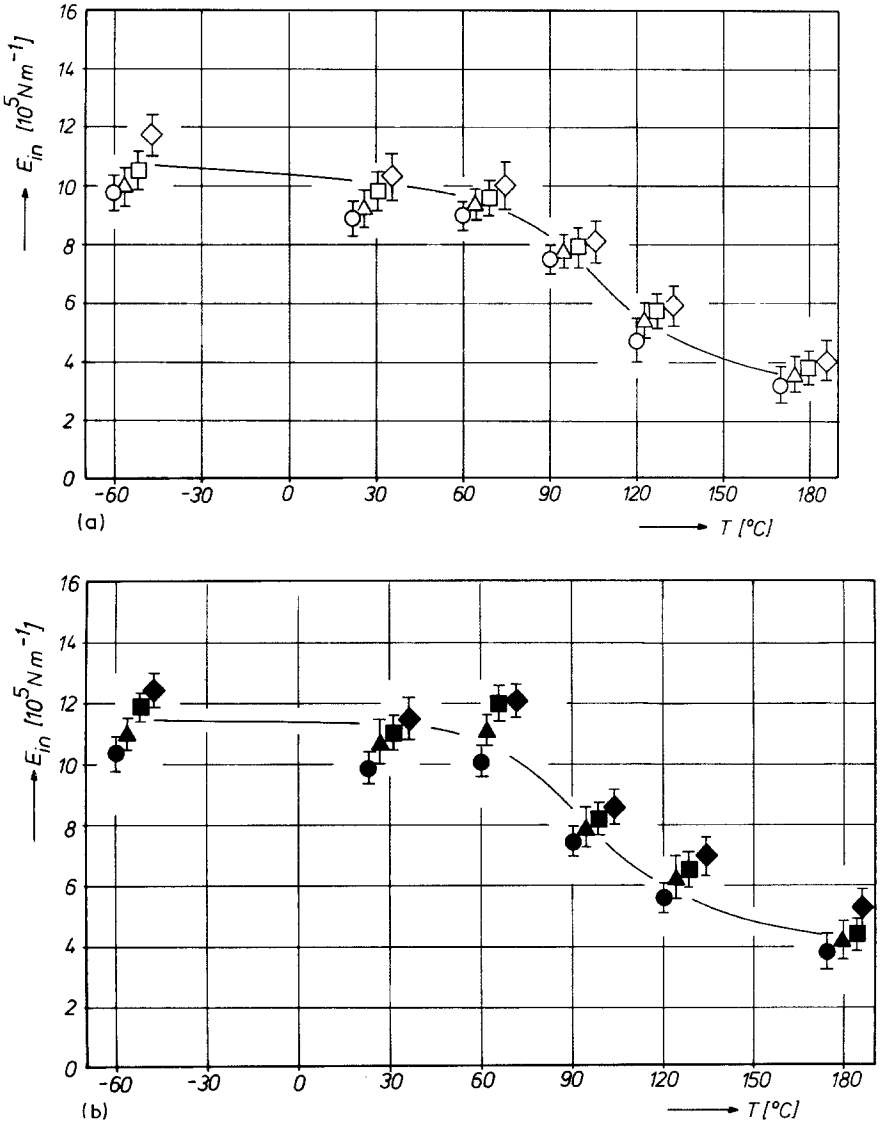

Figure 8 (a) E_{in} against (T, v) curves for the 30% GF-reinforced PPS composite. T-crack; v = (○) 10^0, (△) 10^1, (□) 10^2, (◇) 10^3 mm min^{-1}. (b) E_{in} against (T, v) curves for the 30% CF-reinforced PPS composite T-crack; v = (●) 10^0, (▲) 10^1, (■) 10^2, (◆) 10^3 mm min^{-1}.

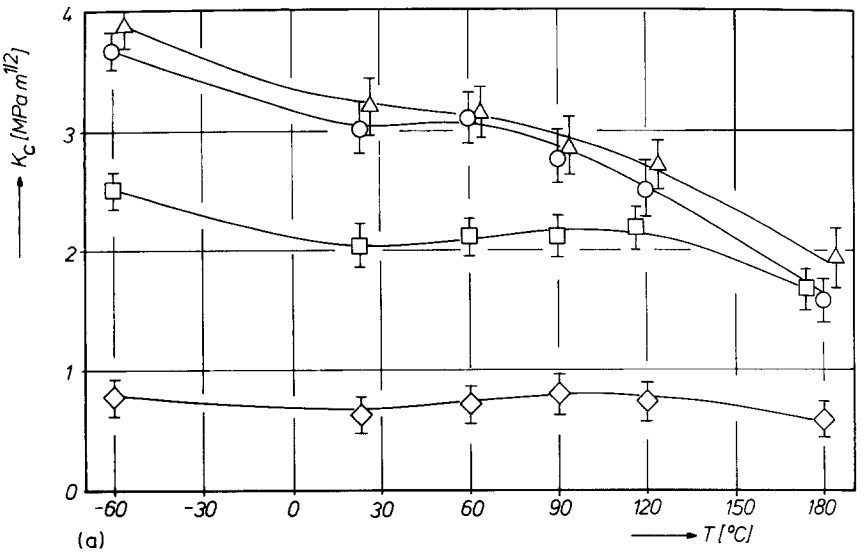

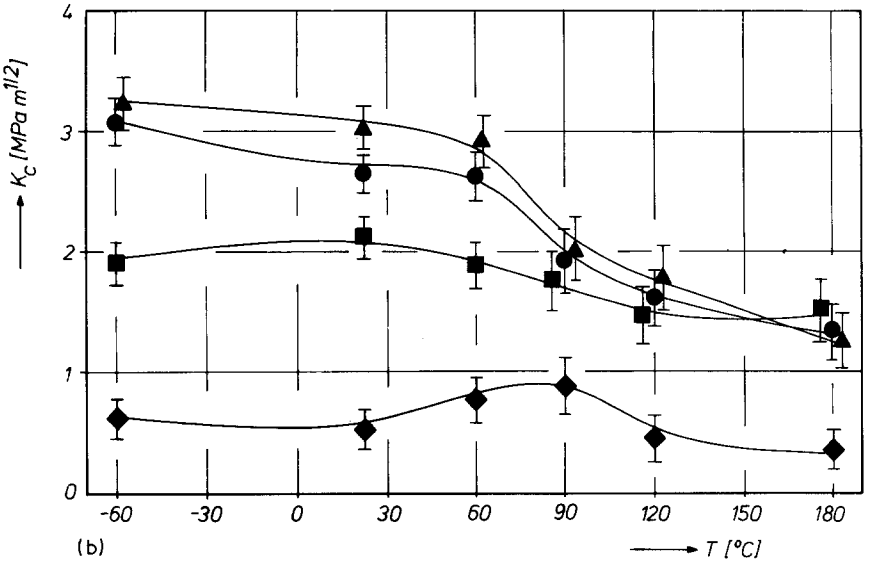

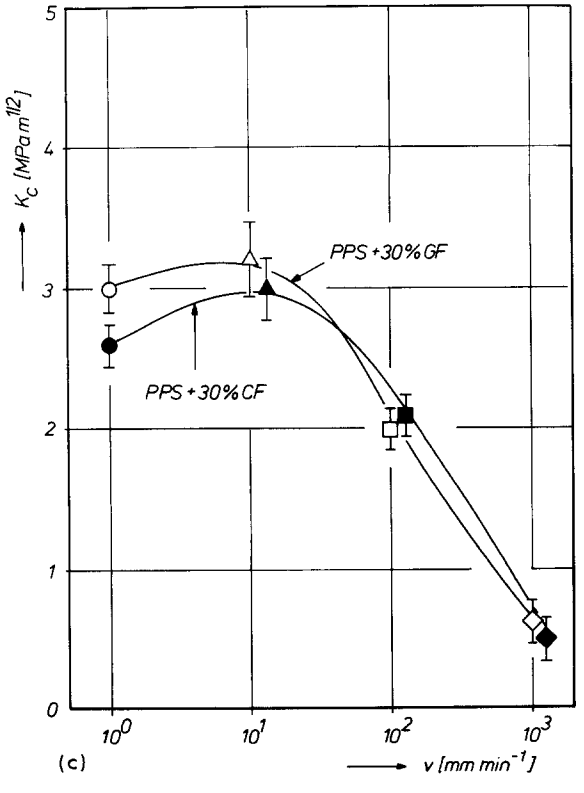

Figure 9 (a) K_c against (T, v) curves for the 30% GF-reinforced PPS composite. T-crack; v = (○) 10^0, (△) 10^1, (□) 10^2, (◇) 10^3 mm min^{-1}. (b) K_c against (T, v) curves for the 30% CF-reinforced PPS composite. T-crack; v = (●) 10^0, (▲) 10^1, (■) 10^2, (◆) 10^3 mm min^{-1}. (c) K_c against v curves at $T = RT$ for the as-received GF- and CF-reinforced PPS, respectively. T-crack.

Instead, a bigger difference is found at very low temperatures, which then reduces permanently with increasing T (Fig. 10b). Calculating from both data sets a fictive fracture energy value, according to

$$G_c^* = K_c^{*2}/E^* \quad (5)$$

a diverging trend between the fibre composite material and the unreinforced polymer with decreasing temperature becomes even more evident (Fig. 11a). This trend is also reflected in the measured values of the "work of failure initiation", W^*, although it occurs in a less pronounced form due to the missing part of deformation and crack propagation energy after exceeding F_c (Fig. 11b). Anyway, from both results it can be concluded that the ability of fibres to cause special mechanisms of energy absorption is absolutely highest when the surrounding matrix is in a relatively

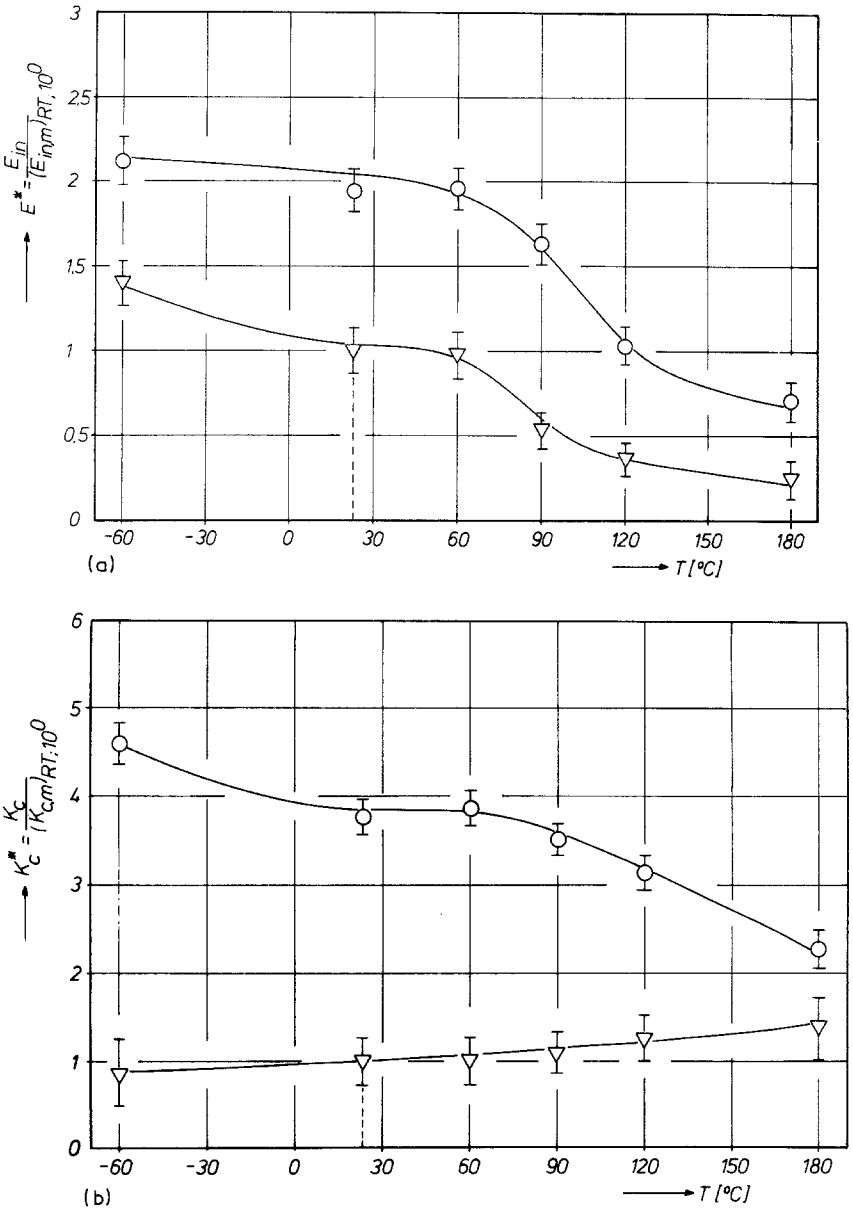

Figure 10 (a) Normalized elastic modulus (E^*) against T curves at $v = 10^0\,\mathrm{mm\,min^{-1}}$ for (▽) the neat and (○) 30% GF-reinforced PPS. The standardization value: $(E_{in,m})_{RT,10^0} = 4.6 \times 10^5\,\mathrm{N\,m^{-1}}$. (b) Normalized fracture toughness (K_c^*) against T curves at $v = 10^0\,\mathrm{mm\,min^{-1}}$ for the (▽) neat and (○) 30% GF-reinforced PPS. The standardization value: $(K_{c,m})_{RT,10^0} = 0.8\,\mathrm{MPa\,m^{1/2}}$). T-crack.

brittle condition. For PPS, the latter situation is highly pronounced for temperatures below $T = 90°\,\mathrm{C}$ ($\simeq T_g$), even when very low testing velocities are applied ($v = 10°\,\mathrm{mm\,min^{-1}}$).

From the designer's point of view it is often of special interest how toughness and modulus of a given material in a reference condition change simultaneously with external testing parameters. A special way to present this information is the construction of fracture toughness maps (Figs 12 and 13). In these maps the fracture toughness is plotted against the elastic modulus of the material, and the different graphs illustrate the changes in both values with temperature (fully drawn lines) or deformation rate (dashed lines). If the values are normalized to any reference condition this type of presentation can easily be used by the designer to find the service restricting parameters of T and v relative to the standard situation. In the present case K_c^{**} is the fracture toughness of the individual composites normalized to their value at $T = RT$ and $v = 10^1\,\mathrm{mm\,min^{-1}}$. The same reference condition was chosen for E^{**}. This means at all values above and on the right-hand side of the 100% field the material proves to be better than when being tested under standard conditions. For all external data pairs lying within the 80% field, at least 80% of the mechanical standard requirements are fulfilled.

3.3. Failure mechanisms

Analysing crack paths on polished sides of compact tension specimens as well as fracture surfaces of the broken CT-samples in the SEM leads to the conclusion that three major failure mechanisms dominate the fracture processes:

1. ductile matrix yielding or brittle matrix fracture;
2. pull-out of fibres, more or less perpendicularly oriented to the crack front;
3. fibre/matrix separation of fibres aligned more parallel to the fracture plane.

Features of fibre fracture can only occasionally be identified. Schematically, the different breakdown mechanisms are illustrated in the centre of Fig. 14. The surrounding fractographic photos, taken from the crack paths (Figs 14a and b) and from the fracture surfaces (Figs 14c and d), respectively, verify the individual failure mechanisms for a selection of different materials and testing conditions. It must be noted, though, that the actual contribution of each of

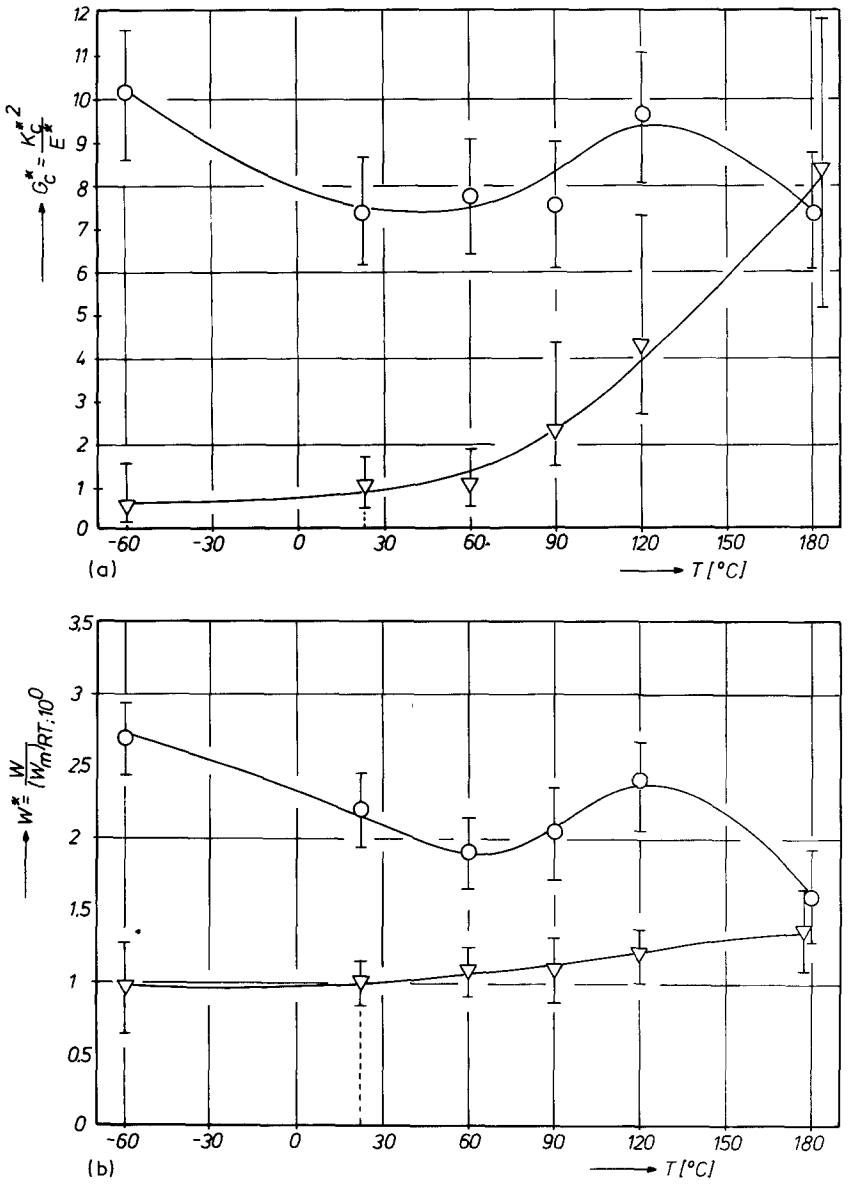

Figure 11 (a) G_c^* against T curves at $v = 10^0$ mm min^{-1} for the (▽) neat and (○) 30% GF-reinforced PPS. T-crack. (b) W^* against T curves at $v = 10^0$ mm min^{-1} for (▽) the neat and (○) 30% GF-reinforced PPS. T-crack. The standardization value $(W_m)_{RT,10^0} = 0.08$ J.

these mechanisms is influenced by the types of fibre reinforcement and matrix modification, by the crack direction (transverse (T) or longitudinal (L) to MFD; only T-cracks are considered), and by the testing temperature (T) and crosshead speed (v).

The effects of the latter parameters on the dominating failure mechanisms can be shown in the form of failure maps for each particular material. A typical example is given in Fig. 15 for the glass fibre-PPS composite. The T against v area can be subdivided mainly into three major portions, A, B and C. In region A, failure of the particle-toughened PPS-matrix used in this composite takes place in a ductile manner. It seems that the matrix separates easily from the fibres, even in regions where fibres are oriented perpendicular to the crack front. Subsequently, the polymer is torn apart after some minor amount of ductile yielding. The fractographic pictures also give the impression that this kind of matrix yielding is preferrably induced at or near fibre ends. Thus, fibre pull-out can only occur along relatively short fibre stumps, and the frictional coefficients during pull-out should be low due to the softened matrix material. In this way, the major contribution to the absorbed energy during the breakdown of the composites should be based on the plastic deformation of the matrix material. In fact, the fracture energies of the unreinforced and reinforced PPS-samples come very close in this range of testing conditions (see Fig. 11a).

Reducing the temperature below the glass transition region of the polymer leads to an embrittlement of the matrix. Under relatively low crack opening rates, brittle fracture can develop rather slowly, starting from and staying mainly in the plane of the initial notch (region B). In this way, an enhanced contribution of fibre pull-out over a longer fibre distance can take place. The specific debonding and frictional forces should also be higher than in region A because of a higher matrix stiffness and higher shrinkage stresses of the matrix on to the fibres. The relative improvement of the G_c^* values of the polymer by fibre reinforcement can be therefore mainly attributed to the fibre induced energy absorbing mechanisms.

A third region, C, can be identified in the failure map mainly for the range of higher crosshead speeds. Here, the spontaneous loading of the samples obviously induces stress concentrations at fibre ends which are high enough to cause multiple brittle matrix cracking.

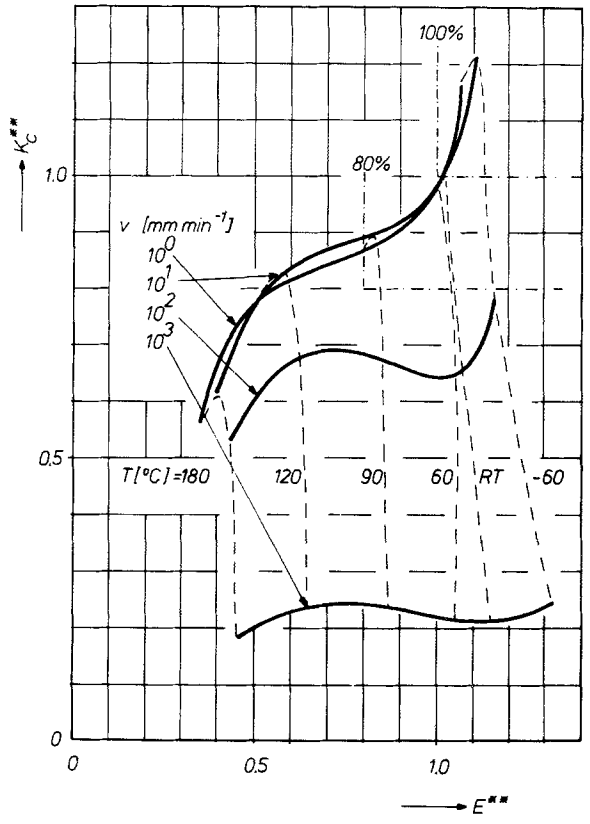

Figure 12 Fracture map (K_c^{**} against E^{**} curves at different temperatures and crosshead speeds) for the 30% GF-reinforced PPS. T-crack. The standardization values: $(K_{c,c})_{RT,10^1} = 4.0\,MPa\,m^{1/2}$; $(E_{in,c})_{RT,10^1} = 9.2 \times 10^5\,N\,m^{-1}$.

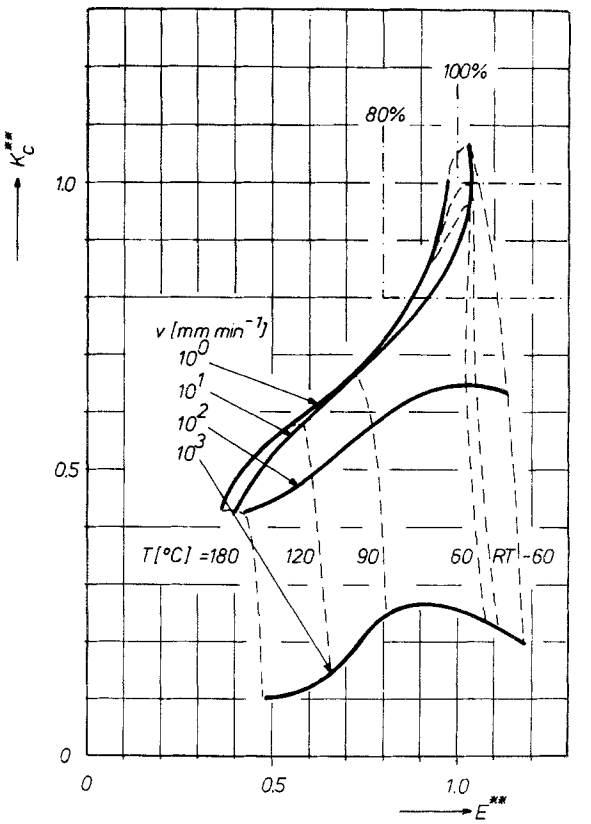

Figure 13 K_c^{**} against E^{**} curves at different temperatures and crosshead speeds for the 30% CF-reinforced PPS, T-crack. The standardization values: $(K_{c,c})_{RT,10^1} = 3.75\,MPa\,m^{1/2}$ $(E_{in,c})_{RT,10^1} = 1.07 \times 10^6\,N\,m^{-1}$.

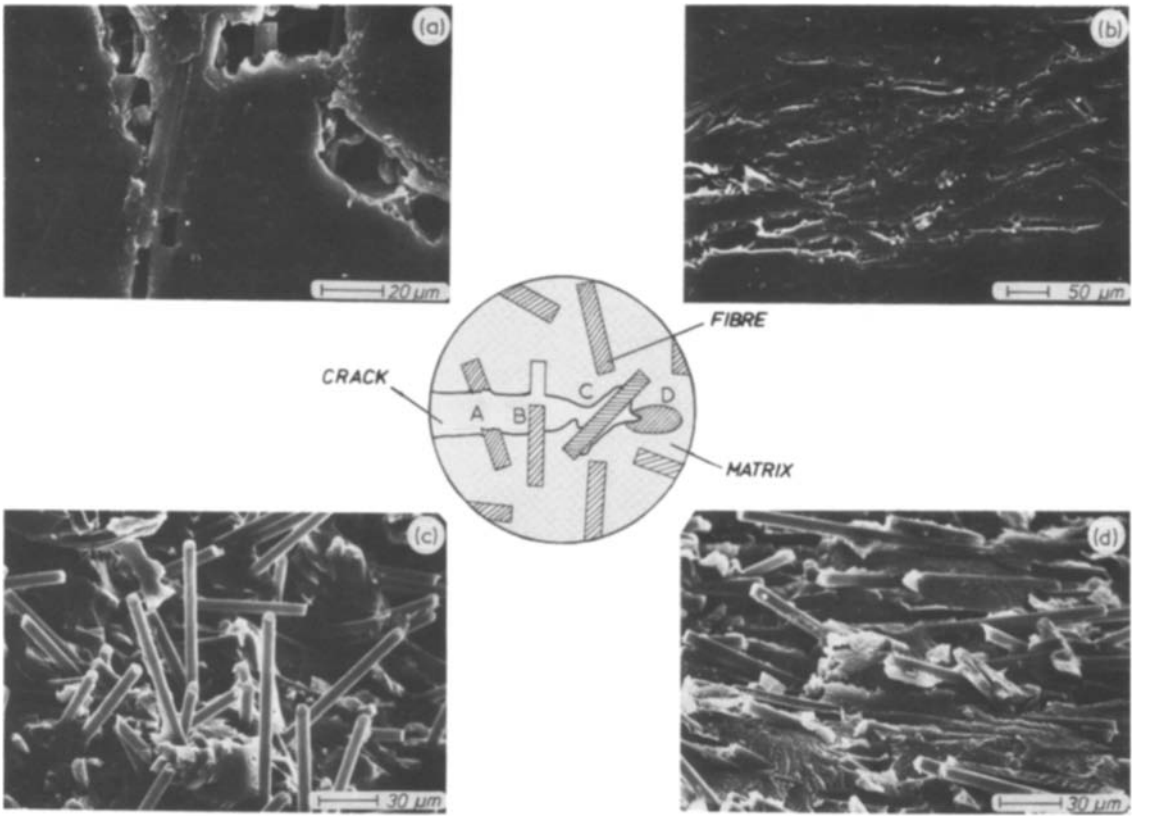

Figure 14 Schematic failure mechanisms for the example of CF reinforced PPS. Testing conditions: (a) $T = -60°\,C$; $v = 10^1\,mm\,min^{-1}$; (b) $T = 180°\,C$; $v = 10^0\,mm\,min^{-1}$; (c) $T = -60°\,C$; $v = 10^0\,mm\,min^{-1}$; (d) $T = -60°\,C$; $v = 10^3\,mm\,min^{-1}$.

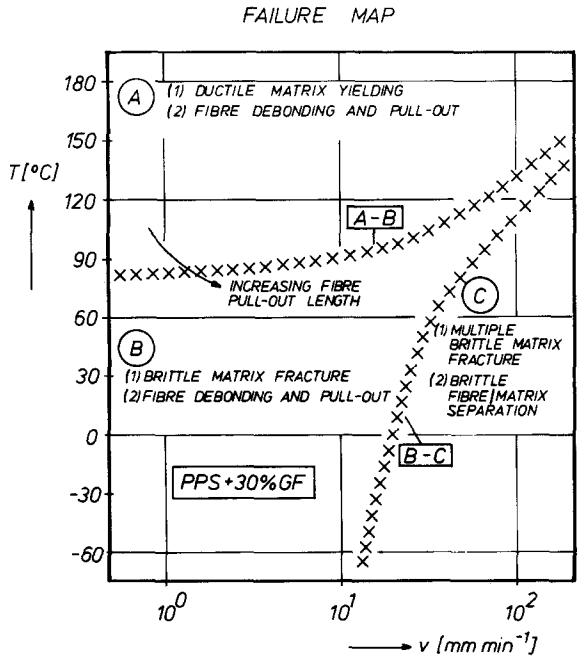

Figure 15 Failure map for the GF-reinforced PPS composite.

The latter events seem to occur simultaneously to the fracture starting from the initial notch, and results in a fracture surface containing many pieces of matrix material broken in a brittle manner. On the one hand, such a multiple matrix fracture should be more favourable than a one-plane brittle fracture with respect to higher fracture energy of the polymer. On the other hand, this trend prevents the possibility of fibre pull-out, a mechanism of high energy absorption. Thus, the fracture energies of the composites should be clearly lower than those measured in the region of lower testing velocities. This transition should be the more pronounced, the lower is the ambient temperature.

For a final comparison, the three principle breakdown processes of the composites within the three different regions of the failure map in Fig. 15 (A, B, C) are schematically illustrated in Fig. 16. For further evidence, typical fracture surface photographs of samples broken under particular testing conditions are added.

With respect to the carbon fibre-PPS composite, similar descriptions of the failure behaviour as given in Fig. 15 can also be performed here. There are, however, some clear shifts in the positions of the borderlines between the individual zones A, B and C (A–B upwards, B–C to the left). These are due to the fact that the matrix used in this composite behaves more brittlely because of the missing toughening particles. An example of the differences in the matrix behaviour is shown in Fig. 17 for CF-PPS at a testing condition of $T = 180°\,C$ and $v = 10^0\,mm\,min^{-1}$. In comparison to the rather ductile matrix failure found for the particle-toughened GF-PPS composites at $T = 180°\,C$, even at $v = 10^2\,mm\,min^{-1}$ (Fig. 16a), the matrix of the CF-PPS in Fig. 17 exhibits a clearly brittle appearance.

3.4. Annealing effects on stiffness and toughness

Finally it should be mentioned that the mechanisms described are, in principle, also valid for the annealed materials. Their slightly higher values of both fracture toughness and elastic modulus at the various testing conditions (Table III) may be explained by two facts:

1. the higher degree of crystallinity (cf. Table I) and corresponding strength of the polymer matrix; and
2. stronger mechanical shrinkage stresses of the more crystalline polymer matrix, causing enhanced debonding forces prior to fibre pull-out.

This unexpected feature of annealing that the thermal treatment improves both the stiffness and the toughness of the PPS composites has also been established by Zeng and Ho [17]. The effect is rather controversial to the general findings relating to semi-crystalline thermoplastics, where stiffness is increased at the cost of toughness during annealing.

4. Conclusions

The findings of the present study on the microstructure–fracture toughness (K_c) relationship of injection-moulded unfilled and short GF- and CF-reinforced PPS composites can be summarized in the following form:

1. Microstructure. The matrix layer structure indicated by DSC thermograms for both the unfilled and reinforced PPS versions depends highly on the processing conditions as well as on the charactristics of the impact modifier eventually used. Annealing does not cause any curing of the PPS, but results in a higher matrix crystallinity and a simplified layer structure pattern.

2. Fracture and failure. The stiffness of both the unfilled and reinforced PPS composites shows a drop

TABLE III Comparison of the normalized fracture toughness (K_c^{**}) and E-modulus (E^{**}) of the as-moulded and annealed PPS composites (for the standardization values at $v = 10^1\,mm\,min^{-1}$ and $T = RT$, cf. Figs 12 and 13, respectively)

Temperature T (°C)	Crosshead speed (mm min^{-1})	PPS + 30% GF				PPS + 30% CF			
		As-moulded		Annealed		As-moulded		Annealed	
		K_c^{**}	E^{**}	K_c^{**}	E^{**}	K_c^{**}	E^{**}	K_c^{**}	E^{**}
RT	10^0	0.95	0.97	1.08	0.98	0.88	0.91	1.22	0.95
	10^1	1	1	1.03	0.98	1	1	1.17	1.05
	10^2	0.63	1.07	0.95	1.06	0.69	1.03	0.80	1.05
	10^3	0.2	1.15	0.15	1.11	0.16	1.10	0.11	1.12
180	10^0	0.58	0.35	0.85	0.40	0.43	0.36	0.59	0.39
	10^1	0.60	0.38	0.88	0.40	0.40	0.38	0.48	0.41
	10^2	0.53	0.43	0.58	0.42	0.51	0.41	0.51	0.43
	10^3	0.18	0.45	0.18	0.45	0.11	0.47	0.13	0.47

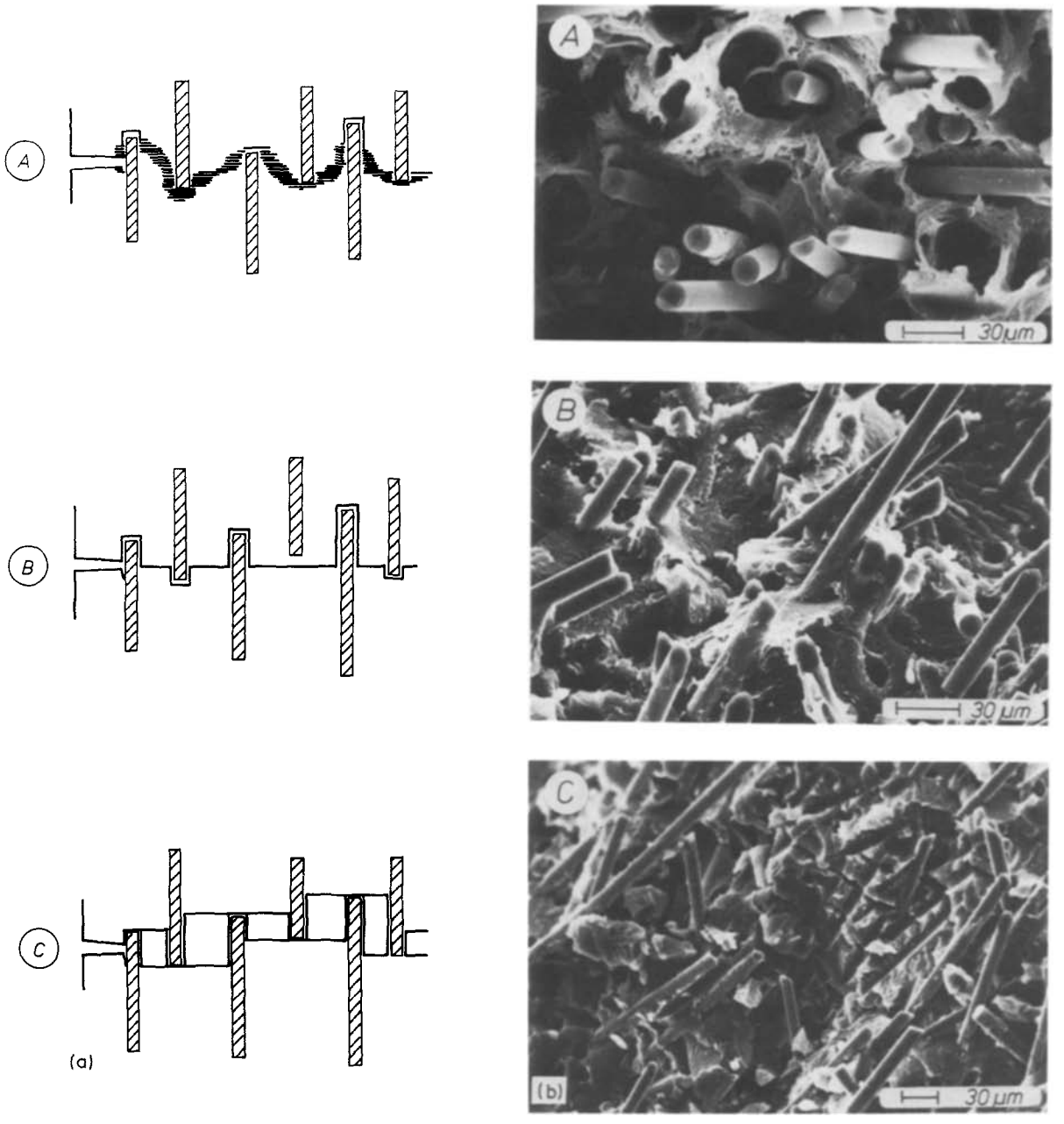

Figure 16 (a) Schematic failure modes proposed for the short fibre reinforced PPS composites. (b) Failure modes observed for the GF-reinforced as-moulded composite. Testing conditions: (A)$T = 180°\,C$; $v = 10^2\,mm\,min^{-1}$; (B) $T = -60°\,C$; $v = 10^0\,mm\,min^{-1}$; (C) $T = -60°\,C$; $v = 10^3\,mm\,min^{-1}$.

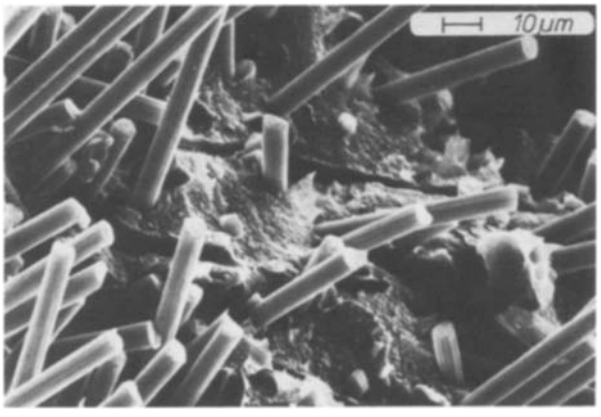

Figure 17 SEM micrograph on the fracture surface of the CF-reinforced PPS composite. Testing conditions: $T = 180°\,C$, $v = 10^0\,mm\,min^{-1}$.

at $T = T_g$ ($= 90°\,C$) and its value practically does not change with crosshead speed. The fracture toughness of the unfilled PPS lies in the range 0.5 to 1 $MPa\,m^{1/2}$ unaffected by the testing conditions. Its value increases by a factor of 3 to 4 below $T = T_g$ in the case of low crosshead speeds ($v = 10^0$ to $10^1\,mm\,min^{-1}$) and of about 2 at $v = 10^2\,mm\,min^{-1}$ for both the 30% fibre containing composites. Passing $T = T_g$, the K_c value of the composites stabilizes at about twice that of the unfilled matrix at $T = 180°\,C$. At higher crosshead speeds, K_c does not significantly change with temperature in a broad range. The curve of the calculated fracture energy as a function of temperature agrees well with that of the evaluated work of failure initiation. Failure of the matrix in the composites occurs ductilely at $T > T_g$, but brittlely below $T = T_g$, in both cases associated with fibre debonding and pull-out

mechanisms. At higher crosshead speeds and below the frequency-dependent T_g, brittle multiple matrix cracking with brittle matrix/fibre separation was seen. Annealing simultaneously upgrades both the toughness and stiffness of the PPS composites.

Acknowledgements

J. Karger-Kocsis thanks the Alexander von Humboldt Foundation for the fellowship at the Polymer and Composites Group of the TU Hamburg-Harburg. Part of the work was supported by the Deutsche Forschungsgemeinschaft (DFG; FR 675/1-1).

References

1. C. F. FRIEDEL and J. M. CRAFTS, *Ann. Chem. Phys.* **14** (1888) 433.
2. P. GRENVESSE, *Bull. Soc. Chim. France* **17** (1897) 599.
3. D. G. BRADY, *J. Appl. Polym. Sci. Appl. Polym. Symp.* **36** (1981) 231.
4. *Idem, J. Appl. Polym. Sci.* **20** (1976) 2541.
5. R. M. BLACK, C. F. LIST and R. J. WELLS, *J. Appl. Chem.* **17** (1967) 269.
6. N. S. J. CHRISTOPHER, J. L. COTTER, G. J. KNIGHT and W. W. WRIGHT, *J. Appl. Polym. Sci.* **12** (1968) 863.
7. G. F. L. EHLERS, K. R. FISCH and W. R. POWELL, *ibid. A-1*, **7** (1969) 2955.
8. R. T. HAWKINS, *Macromol.* **9** (1976) 189.
9. M. WEJCHAN-JUDEK and A. ZUK, *Polym. Degr. Stability* **11** (1985) 55.
10. V. A. SERGEYEV, V. K. SHITIKOV, V. I. NADEL'KIN, A. A. ASKADSKII, K. A. BYCHKO, G. L. SLONIMSKII and V. V. KORSHAK, *Vysokomol. Soedin. Ser. A.* **19** (1977) 1298.
11. H. W. HILL and D. G. BRADY, *Polym. Eng. Sci.* **16** (1976) 831.
12. J. P. JOG and V. M. NADKARNI, *J. Appl. Polym. Sci.* **30** (1985) 997.
13. A. J. LOVINGER, D. D. DAVIES and F. J. PADDEN, *Polymer* **26** (1985) 1595.
14. K. FRIEDRICH, *Compos. Sci. Technol.* **22** (1985) 43.
15. C. LHYMN, *J. Mater. Sci. Lett.* **4** (1985) 1217.
16. C. LHYMN and J. M. SHULTZ, *ibid.* **4** (1985) 1244.
17. H. ZENG and G. HO, *Angew, Makromol. Chem.* **127** (1984) 103.
18. G. AKAY, Flow induced orientation and diffusion in glass fibre reinforced polymer melts in "Interrelation between Processing Structure and Properties of Polymeric Materials", edited by J. C. Seferis and P. S. Theocaris (Elsevier Science, Amsterdam, 1984) p. 669.
19. J. KARGER-KOCSIS and I. CSIKAI, *Polym. Eng. Sci.* **26** (1986) in press.
20. M. ITO and R. S. PORTER, *J. Polym. Sci. Phys.* **23** (1985) 245.
21. B. J. TABOR, E. P. MAGRÉ and J. BOON, *Eur. Polym. J.* **7** (1971) 1127.
22. J. KARGER-KOCSIS and K. FRIEDRICH, *Polymer* **27** (1986) in press.
23. P. J. HOLDSWORTH and A. TURNER-JONES, *ibid.* **12** (1971) 195.
24. V. A. SERGEYEV, V. K. SHITIKOV and V. I. NADEL'KIN, *Vysokomol. Soed. Ser. B.* **19** (1977) 396.
25. G. MENGES and P. GEISBÜSCH, *Coll. Polym. Sci.* **260** (1982) 73.
26. J. M. SCHULTZ and K. FREIDRICH, *J. Mater. Sci.* **19** (1984) 2246.

Received 28 April
and accepted 10 July 1986